

Gibbs Tracking: A Novel Approach for the Reconstruction of Neuronal Pathways

B.W. Kreher,^{1*} I. Mader,^{2,3} and V.G. Kiselev¹

Reconstruction of neuronal fibers using diffusion-weighted (DW) MRI is an emerging method in biomedical research. Existing fiber-tracking algorithms are commonly based on the “walker principle.” Fibers are reconstructed as trajectories of “walkers,” which are guided according to local diffusion properties. In this study, a new method of fiber tracking is proposed that does not engage any “walking” algorithm. It resolves a number of inherent problems of the “walking” approach, in particular the reconstruction of crossing and spreading fibers. In the proposed method, the fibers are built with small line elements. Each line element contributes an anisotropic term to the simulated DW signal, which is adjusted to the measured signal. This method demonstrates good results for simulated fibers. A single in vivo result demonstrates the successful reconstruction of the dominant neuronal pathways. A comparison with the diffusion tensor imaging (DTI)-based fiber assignment with continuous tracking (FACT) method and the probabilistic index of connectivity (PICO) method based on a multitensor model is performed for the callosal fibers. The result shows a strong increase in the number of reconstructed fibers. These almost fill the total white matter (WM) volume and connect a large area of the cortex. The method is very computationally expensive. Possible ways to address this problem are discussed. Magn Reson Med 60:953–963, 2008. © 2008 Wiley-Liss, Inc.

Key words: diffusion; DTI; fiber crossings; fiber tracking; multi tensor; spatial point process; MCMC

The term “fiber tracking” encompasses a set of methods for the reconstruction of neuronal pathways that use information about the anisotropic diffusion of water molecules in the fibrous structure of white matter (WM) (1). All of these methods include two main steps: measurement of the anisotropic diffusion-weighted (DW) signal as a function of the direction of the DW gradients (2), and reconstruction of the neuronal fibers given the measurement result. In this study, we focus on the latter step, assuming a sufficiently dense sampling of the angular dependence of the signal.

The directions of fast diffusion are associated with the direction of a fiber bundle present in a given voxel. The signal can be described by a single diffusion tensor (DT) in the simplest case of parallel fibers, such as in the truncus

of the corpus callosum. The tensor determines a single direction of the fastest diffusion that reflects the local orientation of the neuronal fibers. The diffusion anisotropy has a more complex pattern in voxels with crossing fibers. This complicates the relation between the signal and the underlying fiber structure, and gives rise to more advanced signal models (3–11).

The main approach of the current methods of fiber tracking (4,10,12–17) is the reconstruction of long neuronal pathways in small successive steps by following the local, voxelwise-defined fiber direction. Starting from local information of the diffusivity, long-distance connections are determined. This method is inherently prone to instability, since an error at a single crossing radically affects the final result.

In this work we present a method based on a new principle: instead of walking successively through the volume, all neuronal pathways and the totality of the signal are taken into account simultaneously. In contrast to other methods, a configuration of all fiber tracks inside the investigated area is determined that explains the underlying measured data in respect to the applied a priori knowledge. This novel approach can reconstruct both crossing and spreading fiber configurations. The method includes three main steps: creation of a trial fiber configuration, calculation of the corresponding DW signal, and adjustment of the trial configuration to the experimentally measured signal to minimize the difference.

This process can be explained by using a close analogy with the chemical reaction of polymerization. The building elements of reconstructed fibers are small straight cylinders whose length, position, and orientation can vary continuously (Fig. 1). The reconstruction begins with cylinders randomly distributed in WM. This state can be compared with a solution of chemical monomer. The interaction between them results in the building of long polymer chains with a low branching probability. The chains, which represent the neuronal fibers, can start and end on predefined surfaces, for example at the boundary with gray matter (GM). Each cylinder contributes a signal typical for parallel fibers to all voxel it crosses. The sum of these contributions in each voxel simulates the anisotropic part of the signal. The requirement of similarity between this signal and the measured one is analogous to an external field acting on the cylinders and forcing them to take locally specific orientations and densities.

The system described is initially taken at high temperature, which is slowly decreased during the simulations to ensure the independence of the initial state and to find the optimal final configuration (18). As in real chemical reactions, the monomers change their configuration to minimize free energy. We name the described method “Gibbs tracking,” keeping in mind its close analogy to statistical physics. The method is actually a Bayesian approach,

¹Medical Physics, Department of Diagnostic Radiology, University Hospital, Freiburg, Germany.

²Section of Neuroradiology, Neurocenter, University Hospital, Freiburg, Germany.

³Freiburg Brain Imaging Center, Department of Neurology, University Hospital, Freiburg, Germany.

Presented in part at the 15th Annual Meeting of ISMRM, Berlin, Germany, 2007.

*Correspondence to: Dr. Björn Wolf Kreher, Medical Physics, Dept. of Diagnostic Radiology, University Hospital Freiburg, Hugstetter Str. 55, D-79106 Freiburg, Germany. E-mail: bkreh@web.de.

Received 1 November 2007; revised 8 June 2008; accepted 11 June 2008.

DOI 10.1002/mrm.21749

Published online in Wiley InterScience (www.interscience.wiley.com).

© 2008 Wiley-Liss, Inc.

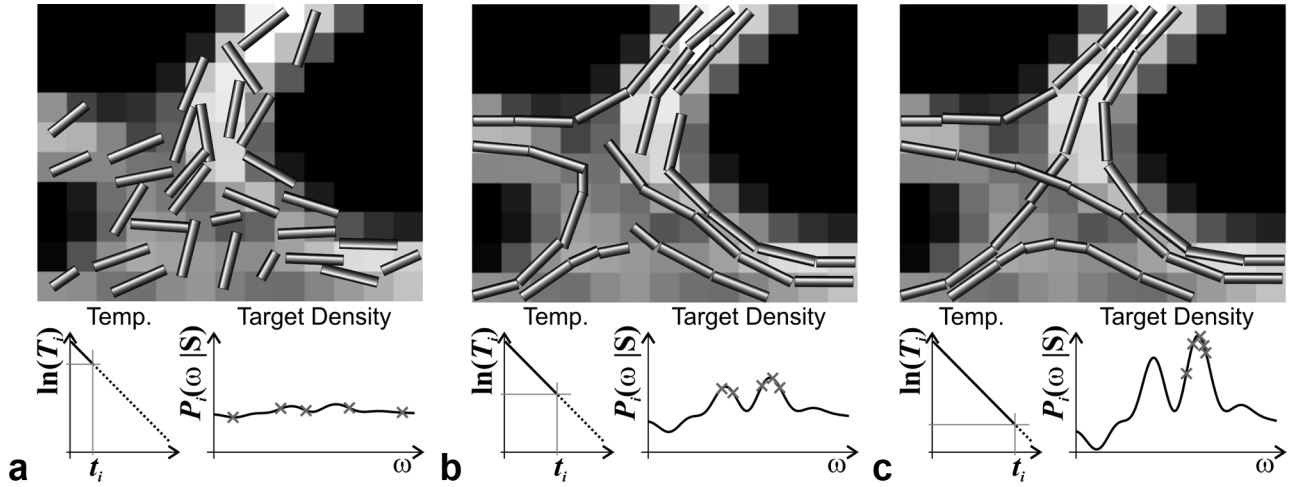


FIG. 1. Principle of the Gibbs tracking method. **a:** For very high temperatures, the target density curve is relatively flat. Therefore, the configuration of cylinders is nearly arbitrary and without structure. **b:** For lower temperatures, the target density is sharper and the samples are more often in areas of higher probability, resulting in more structured but still variable cylinder configurations. **c:** For temperatures close to zero, the target density is very narrow. Due to the dependence on the predecessor of the RJMCMC, only samples that are inside a local extremity are drawn. Hence, the cylinder configurations are very structured and only small changes are possible.

based on spatial point processes (19). From this point of view, the interaction between the cylinders represents the a priori probability, and the similarity between the measured and simulated signals determines the likelihood function. Note that this method is inspired by the so-called Candy model (20), which is used for road recognition in remotely acquired terrain images.

This work is structured as follows: The next section provides details of the method described above. The Gibbs tracking is tested by two simulated phantoms and a single in vivo measurement in the human brain. A comparison among Gibbs tracking, the DTI-based fiber assignment with continuous tracking (FACT) method, and the probabilistic index of connectivity (PICO) method based on a two component multi-DT (MDT) model is done for callosal fibers as an example. The parameters and properties are briefly described in the Materials and Methods section and the outcomes are shown in the Results section. A discussion completes the report.

MATERIALS AND METHODS

The Gibbs tracking method relies on the piecewise approximation of neuronal pathways by small cylinders. Each cylinder is defined by the tuple $h_i = (\mathbf{r}_i, m_i)$. The three-dimensional vector $\mathbf{r}_i = (x_i, y_i, z_i)$ specifies the center of the cylinder, and $m_i = (l_i, \theta_i, \phi_i)$ defines its length $l_{\min} \leq l_i \leq l_{\max}$ and orientation by the polar angle $-\frac{1}{2}\pi \leq \theta_i < \frac{1}{2}\pi$ and the azimuth angle $0 \leq \phi_i < \pi$ (Fig. 2a). The radius $r_{\text{cyl}} > 0$ is predefined and identical for all cylinders. The two ends \mathbf{a}_i^+ and \mathbf{a}_i^- of the cylinder h_i are calculated by:

$$\mathbf{a}_i^+ = \mathbf{r}_i + \frac{l_i}{2} \begin{pmatrix} \cos \phi_i \cos \theta_i \\ \sin \phi_i \cos \theta_i \\ -\sin \theta_i \end{pmatrix} \quad \mathbf{a}_i^- = \mathbf{r}_i - \frac{l_i}{2} \begin{pmatrix} \cos \theta_i \cos \theta_i \\ \sin \phi_i \cos \theta_i \\ -\sin \theta_i \end{pmatrix}. \quad [1]$$

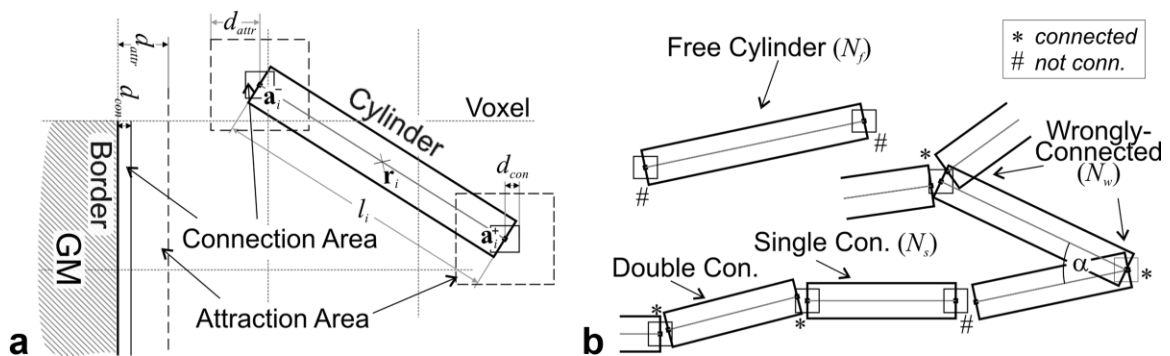
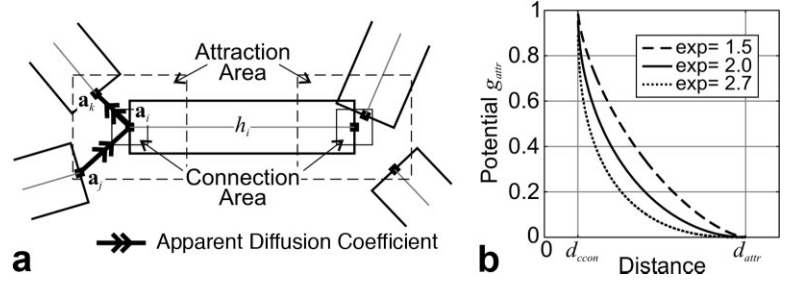


FIG. 2. Basic elements and states of the Gibbs tracking method. **a:** The border planes are predefined and mark the transition between GM and WM. The cylinders provide a piecewise approximation of the fiber trajectories. Connection and larger attraction areas surround the border planes at the ends of the cylinders. The rectangular shape of the connection areas is due to the selected maximum norm. **b:** The different connecting states of the cylinders (single, double, wrongly-connected, and free) are shown.

FIG. 3. Attraction relation between cylinders. **a**: Examples of the asymmetric attraction relation. Here, \mathbf{a}_j is attracted by \mathbf{a}_i and \mathbf{a}_i is attracted by \mathbf{a}_k . **b**: Attraction potential for different exponents as function of the distance of the attracting extremities.



Additionally, there are predefined border planes, marking the transition between white and grey matter. The border-planes are aligned to the grid and lie on the border surface of two neighbouring voxels (Fig. 2a). The method introduced here aims to find a set of cylinders $\omega = \{h_1, \dots, h_n\}$, which approximate the underlying fiber pathways. We will also refer to this set as a configuration of cylinders. The probability of a given configuration of cylinders, ω , is defined in the form similar to the microscopic energy in the Gibbs distribution in statistical physics:

$$f_T(\omega) = \exp\left(-\frac{1}{T} U_I(\omega)\right) \exp\left(-\frac{1}{T} U_D(\omega, \hat{\mathbf{S}})\right). \quad [2]$$

Here, U_I represents the interaction energy (or internal energy) of a given configuration ω independently of the measured data; U_D corresponds to the data energy (external energy) and scores how well the configuration ω explains the measured data $\hat{\mathbf{S}}$; and T is the overall temperature of the system. In the context of Bayesian statistics, the potential function $f_T(\omega)$ can be seen as a non-normalized a posteriori probability at the temperature T . The term $\exp\left(-\frac{1}{T} U_I(\omega)\right)$ defines the a priori probability and $\exp\left(-\frac{1}{T} U_D(\omega, \hat{\mathbf{S}})\right)$ defines the likelihood function. The energy functions U_I and U_D are described in more detail in the following two sections.

Interaction Energy

The interaction energy favors the formation of the cylinders into chains, with a structure similar to that of neuronal fibers. It is assumed that 1) neuronal fibers connect functional areas (lying in the GM) with other functional areas (e.g., the association fibers) or that they leave the brain (e.g., projecting fibers); 2) neuronal pathways generally have a smooth trajectory; and 3) single axons do not branch.

The interaction energy is expressed in terms of the number of cylinders in different states defined according to their position relative to other cylinders and boundaries. First, we define small connection areas of size d_{con} around both ends of each cylinder and close to the border-planes (Fig. 2a). A cylinder is connected if its end is inside the connection area of another object (Fig. 2b). It is a single or a double connection depending of the number of connected ends. A cylinder is wrongly connected if the connection results in a sharp angle in the cylinder chain or there are two cylinder ends inside its connection area. The

latter condition takes into account the fact that the real axons do not branch.

A larger attraction area of the size d_{attr} (Fig. 3) is defined around each connection area. In this area, two endpoints are attracted with the energy

$$g_{attr}(\mathbf{a}_i, \mathbf{a}_j) = 1 - \left(1 - \frac{(d_{attr} - \|\mathbf{a}_i - \mathbf{a}_j\|_x)^q}{(d_{attr} - d_{con})^q}\right)^{\frac{1}{q}}. \quad [3]$$

Here, the distance is measured as the maximum norm, $\|\cdot\|_x$, defined as the maximum of the three Cartesian components. The exponent q is a predefined constant, influencing the shape of the potential function as shown in Fig. 3b. We have selected $q = 2$. This interaction is switched off if one of the endpoints is connected, or is not the closest neighbor of the other. This interaction is not symmetric.

In summary, the interaction energy takes the form:

$$U_I(\omega) = w_f N_f(\omega) + w_s N_s(\omega) - w_a W_a(\omega) + w_w N_w(\omega). \quad [4]$$

The terms w_f , w_s , w_a and w_w are positive weights that influence the priority of the different criteria (Table 1). The firm value $w_s = 1$ sets the unit of energy accepted in this study. N_f , N_s and N_w are the numbers of free, single connected, and wrongly-connected cylinders, respectively. Energy $W_a(\omega)$, is the sum of g_{attr} (Eq. [3]) for all attracting pairs in ω . The requirement of building connected chains

Table 1
List of Parameters Used for the Gibbs Tracking Model

Parameter name	Type	Values
Eigenvalues of tensor component	A	[1.7;0.2;0.2] $\mu\text{m}^2/\text{ms}$
Radius of the cylinders r_{cyl}	A	0.3 mm
Length of connection area d_{con}	A	0.075 mm
Length of attraction area d_{attr}	A	0.75 mm
Interval of cylinder length l_{min} and l_{max}	A	1-4 mm
Threshold for angle criteria α_w	P	120°
Intensity of Poisson process β	P	0.2 mm^{-4}
Penalization of free cylinders w_f	P	2.2
Penalization of single connected cylinders w_s	P	1.0
Favoring attraction cylinder ends w_a	P	0.5
Penalization of wrongly-connected cylinders w_b	P	4.0

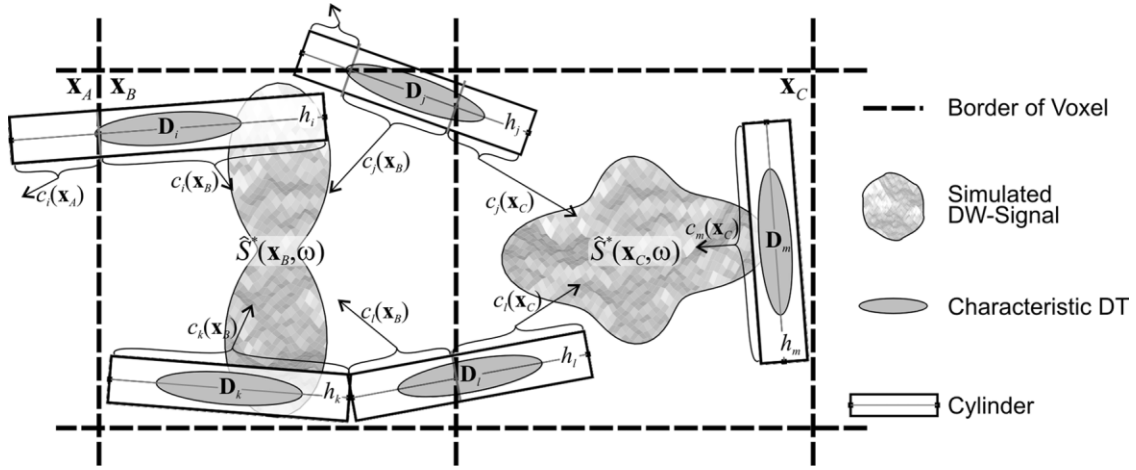


FIG. 4. Simulation of the DW signal by a configuration of cylinders with the adaptive MDT model used by the Gibbs tracking model. The number of tensor components is derived from the number of cylinders inside a voxel. The signal fraction is defined by the volume fraction of the cylinders in the voxel. For example, $c_i(\mathbf{x}_A)$ is the volume fraction of the cylinder h_i inside the voxel \mathbf{x}_A . The eigenvalues of the tensor components are predefined and the eigenvectors are calculated using the orientation of the cylinders.

imposes constraints on the parameters: $w_s > w_a$ and $w_f > w_s + w_a$.

Data Energy

The data energy scores how well the measured data $\hat{\mathbf{S}}$ can be explained by a configuration of cylinders ω . An MDT model is used to simulate the DW signal for a given configuration ω . Hereafter the signal is normalized on unity for $b = 0$. The simulation is performed for every voxel inside the WM and for every diffusion-encoding direction. By comparing the measured signal with the simulated one, the data energy is calculated and used to determine the likelihood.

The MDT model used is similar to the one described in Ref. 10. The eigenvalues of all tensor components are predefined and identical, while orientations are defined by the cylinders (Fig. 4). Let \mathbf{x} specify a voxel inside the WM, and \mathbf{B}_k be the b -matrix, corresponding to the k^{th} diffusion-encoding direction. The signal, $\hat{\mathbf{S}}_k^*(\mathbf{x}, \omega)$, is simulated by the following expression:

$$\hat{\mathbf{S}}_k^*(\mathbf{x}, \omega) = \sum_{i=1}^{N(\omega)} c_i(\mathbf{x}) \exp(-\text{Tr}[(\mathbf{B}_k - \mathbf{B}_0)\mathbf{D}_i]) \text{ with} \\ \mathbf{D}_i = \mathbf{R}_z(\phi_i) \mathbf{R}_y(\theta_i) \begin{pmatrix} \lambda_1 & 0 & 0 \\ 0 & \lambda_{2,3} & 0 \\ 0 & 0 & \lambda_{2,3} \end{pmatrix} \mathbf{R}_y(-\theta_i) \mathbf{R}_z(-\phi_i). \quad [5]$$

Here, $N(\omega)$ is the total number of cylinders in the configuration ω ; $\mathbf{R}_z(\phi_i)$ is the rotation matrix on angle ϕ around the z -axis etc.; and \mathbf{D}_i is the DT generated by the cylinders h_i , according to its current orientation (θ_i, ϕ_i) . In each voxel \mathbf{x} the weight c_i of the DT contributed by a given cylinder is assumed to be equal to the volume fraction of this cylinder in the voxel (Fig. 4). The volume of a cylinder in the voxel is defined by the length of the cylinder axis lying in the voxel \mathbf{x} multiplied with πr_{cyl}^2 , where r_{cyl} is the cylinder radius. The cylinders may overlap. For all cylinders outside the voxel, the signal fraction $c_i(\mathbf{x})$ is set to zero. Thus,

the number of components of the MDT model is equal to the number of cylinders inside the current voxel.

The data energy depends on the difference between the measured and the simulated signal, and is calculated using the following formula:

$$U_D(\omega) = u \sum_{\mathbf{x} \text{ in WM}} \sum_{k=1}^I [(\hat{\mathbf{S}}_k^*(\mathbf{x}, \omega) - \overline{\hat{\mathbf{S}}_k^*(\mathbf{x}, \omega)}) - (\hat{\mathbf{S}}_k(\mathbf{x}) - \overline{\hat{\mathbf{S}}_k(\mathbf{x})})]^2. \quad [6]$$

Here, $\hat{\mathbf{S}}_k(\mathbf{x})$ and $\hat{\mathbf{S}}_k^*(\mathbf{x}, \omega)$ are the measured and simulated signals, respectively. The bar denotes averaging over all diffusion-encoding directions. The normalization constant u is selected in such a way that a 10° error in the cylinder orientation contributes unity to U_D .

Minimization of Total Energy

To maximize the a posteriori probability $f_T(\omega)$ (Eq. [2]), we employ a reversal jump Monte Carlo Markov chain (RJMCMC) (21–23) combined with the simulated annealing (24,25). The simulated annealing implies a successive decrease in the system temperature T from a high starting temperature T_0 to a low final temperature T_f during the sampling of state space Ω (Fig. 1). In the present method, the last configuration ω_f after reaching the final temperature T_f is used as the result. In Refs. 18 and 25, the convergence of this class of algorithm was demonstrated for a geometric cooling schedule.

RJMCMC is a sampler that draws a series of configurations $(\omega_0, \dots, \omega_t, \omega_{t+1}, \dots)$ according to a given probability density function, such as the potential function $f_T(\omega)$. These configurations form a chain of points in the state space Ω of all possible configurations. In this chain, the next element depends only on its predecessor. Appending a new element is a small step in Ω , which is performed randomly and then either accepted or rejected. In princi-

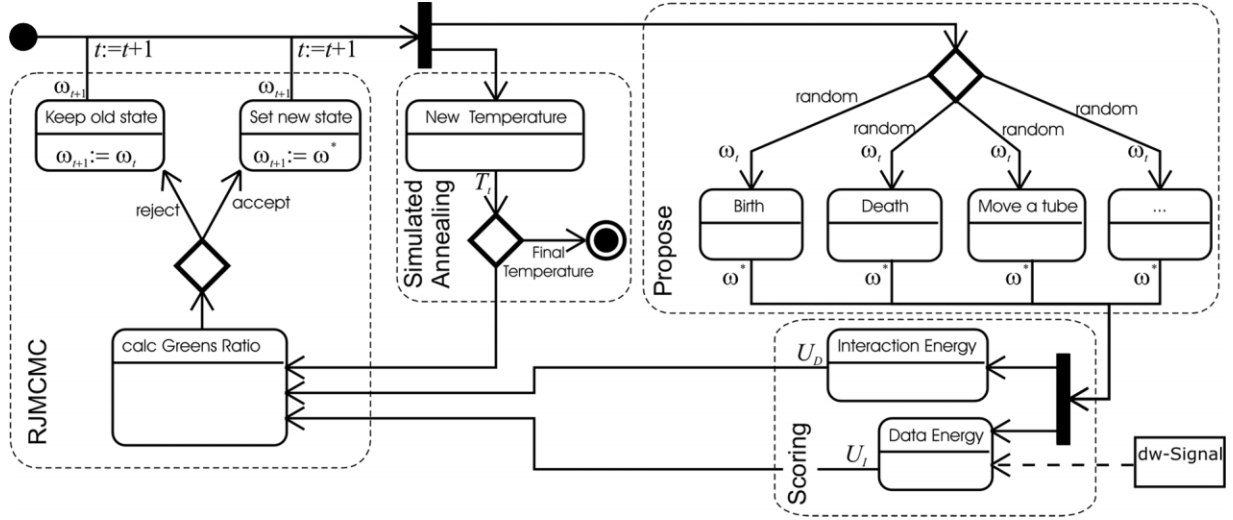


FIG. 5. Machine state diagram of the Gibbs tracking method. New candidates for the next cylinder configuration are drawn using one of the different proposals (Propose block). The candidate is scored using the interaction energy U_I and the data energy U_D , (Scoring block). Additionally, the temperature of the system regarding the simulated annealing procedure is calculated (Simulated Annealing block). The RJMCMC sampler calculates the Green's ratio (RJMCMC block), which defines the probability of the proposed candidate being taken as the new configuration. The counter is then incremented by one, and the loop starts again until the final temperature is reached.

ple, two elementary proposals are sufficient: append a new randomly drawn cylinder to the current configuration (Birth) and remove one cylinder from the current configuration (Death). For computational efficiency, we enlarged the choice of proposals to include several combined steps:

- Birth and Death of a cylinder
- Birth and Death of a single connected cylinder
- Moving one or both ends of a cylinder
- Connect/disconnect two attracting/connected cylinders

An overview of the whole procedure is shown in Fig. 5 as a machine state diagram.

A new candidate, ω^* , given a current configuration ω_t is accepted with a probability equal to the so-called Green's ratio (22,26):

$$R = \frac{f_T(\omega^*)}{f_T(\omega_t)} \frac{q(\text{choosing inv.prop.})}{q(\text{choosing prop.})} \frac{p(\omega^* \rightarrow \omega_t)}{p(\omega_t \rightarrow \omega^*)}. \quad [7]$$

Here, q is the probability of selecting a specific proposal type from the above list. The expression $p(\omega_t \rightarrow \omega^*)$ and $p(\omega^* \rightarrow \omega_t)$ describes the probability density for the step of a given proposal type in the state space Ω from the state ω_t to the ω^* and for the inverse step from ω^* to ω_t , respectively. The determinant of the Jacobi matrix, which is present in the general formula (22,26), equals unity for our selection of parameters.

In the following, the two proposals—Birth and Death of a cylinder—and their determination of the Green's ratio are described as examples. Further general examples for more complex and tailored proposals can be found in (20,27,28).

Birth and Death of a Cylinder

With the application of the Birth operation, a new cylinder h^* is appended to the current configuration ω_t giving rise

to a new candidate configuration ω^* . In our implementation, the length, orientation, and position of the new cylinder h^* are drawn randomly and uniformly within the predefined limits. The associated probability density takes the form $p(\omega_t \rightarrow \omega^*) = [\beta \pi^2 V_{WM} (I_{\max} - I_{\min})]^{-1}$, where the constant β defines the expected mean cylinder density, and V_{WM} is the volume of the WM mask. The inverse step $\omega^* \rightarrow \omega_t$ is the Death of the cylinder h^* . Let $N(\omega^*)$ be the total number of cylinder in ω^* . The probability for removing h^* from ω^* results from $p(\omega^* \rightarrow \omega_t) = N(\omega_t)^{-1}$. The Green's ratio for the Birth proposal is given by

$$R(\omega_t, \omega^*) = \frac{f_T(\omega^*)}{f_T(\omega_t)} \frac{p_d}{p_b} \frac{V_{WM} (I_{\max} - I_{\min}) \pi^2}{N(\omega^*)}. \quad [8]$$

The potential function f_T scores the given configuration (see Eqs. [2], [4], and [6]) and the parameters p_b and p_d are probabilities for choosing the Birth and the Death move, respectively. The Green's ratio for the Death proposal is given by the inverse of the right-hand side of Eq. [8].

Data Generation and Processing

The Gibbs tracking method was implemented in C++. For all results presented here, the initial configuration ω_0 was the empty set. The parameters generally used for Gibbs tracking are listed in Table 1. Inherently, the Gibbs tracking method represents all pathways in the considered volume. Specific fiber bundles are selected as all fibers crossing or ending at specially assigned regions of interest (ROIs).

Simulated Data

The Gibbs tracking method was tested in two simulated data sets, which are referred to as phantoms in the following. For both phantoms, the DW signal was simulated for 60 evenly distributed diffusion-encoding directions with a b -value of 1500 s/mm^2 . The signal was simulated by a

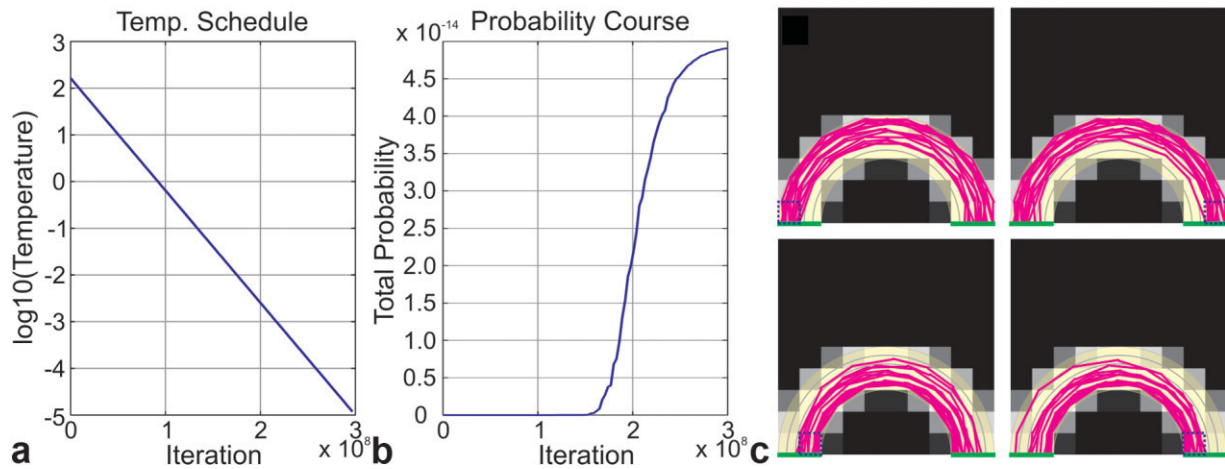


FIG. 6. Results of the Gibbs tracking method applied to the curved phantom. **a**: Applied temperature schedule. **b**: Course of the non-normalized a posteriori probability as a function of the iteration. **c**: Structure and reconstruction results of the simulated phantom. The simulated pathways are indicated by the light yellow area, the border planes were predefined at the green lines, and the resulting trajectories are displayed in magenta. For verification, some of the determined trajectories were selected using the ROIs framed in blue, and visualized in the four maps. [Color figure can be viewed in the online issue, which is available at <http://www.interscience.wiley.com>.]

multicompartment model. A fiber bundle was assigned the properties of a DT with the eigenvalues of $[1.7; 0.2; 0.2]$ $\mu\text{m}^2/\text{ms}$ according to the characteristics of the splenium (29). The background of the phantom was characterized by an isotropic diffusivity of $3.19 \mu\text{m}^2/\text{ms}$, which is typical for cerebrospinal fluid (CSF) (29).

The first phantom contains a curved fiber bundle shaped as a semicircle. It was simulated on a 10×10 grid (Fig. 6c). The signal fraction of the fiber bundle was set to 90%. The border was defined at the edges of the voxel where the bundle leaves the volume. Gibbs tracking was applied to the phantom using a geometric cooling schedule starting

from the initial temperature of $T_0 = 3 \times 10^3$ and reaching the final temperature $T_f = 10^{-5}$ after $J = 3 \times 10^8$ iterations (Fig. 6a).

The second simulated phantom contains a 60° fiber crossing (Fig. 7c). The weight of each fiber bundle was set to 40%. To investigate the dependence between quality of the result and the calculation time, Gibbs tracking was performed several times using different numbers of iterations. For each repetition, the cooling schedule was adapted to start $T_0 = 3 \times 10^3$ and reach the final temperature $T_f = 10^{-5}$ after $J = 10^4; 2 \times 10^4; 5 \times 10^4; 1 \times 10^5; \dots; 3 \times 10^8$ iteration.

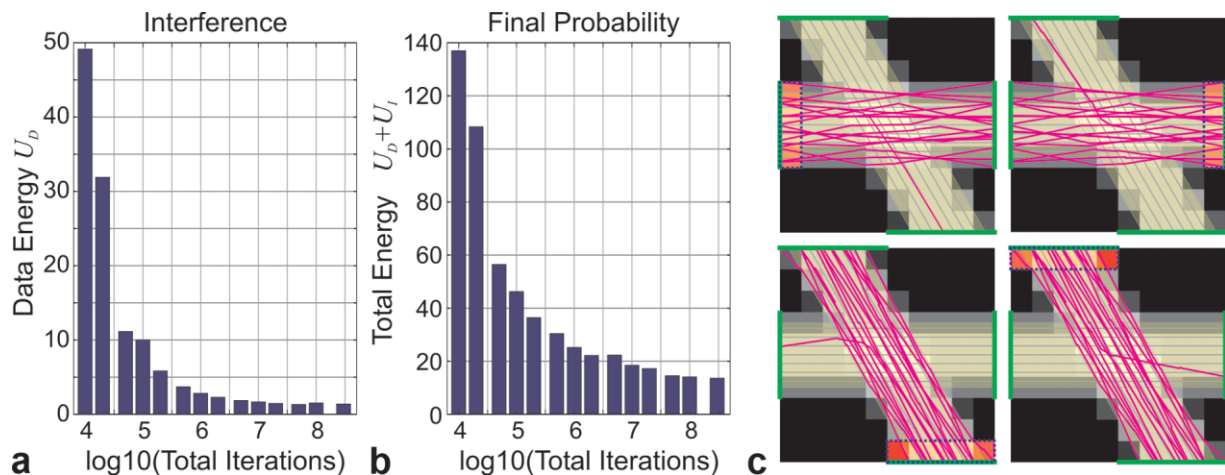


FIG. 7. Results of the Gibbs tracking method applied to the phantom containing 60° crossings. Several temperature schedules with varying iterations were used for by the Gibbs tracking method. The data energy (**a**) and the total energy (**b**), while reaching the final temperature, are plotted against the iteration numbers of the different temperature schedules. Each bar represents the final configuration of a single reconstruction run with the Gibbs tracking method. **c**: The structure and reconstruction results of the simulated phantom. The pathways are indicated by the light yellow area, the border planes were predefined at the green lines, and the resulting trajectories, after applying the temperature schedule with 3×10^8 iterations, are displayed in magenta. For clarity, the determined trajectories were selected using the ROIs framed in blue and overlaid under in red, and visualized in the four maps. [Color figure can be viewed in the online issue, which is available at <http://www.interscience.wiley.com>.]

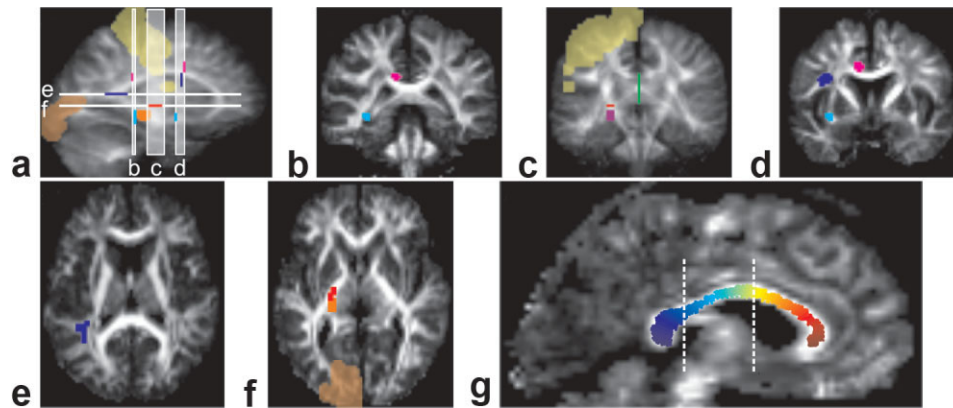


FIG. 8. ROIs created for the selection of fiber bundles. Yellow → motor cortex, red → corticospinal tract, magenta → cingulum, blue → arcuate fasciculus, cyan → inferior fronto-occipital fasciculus, green → corpus callosum, orange → visual cortex/lateral geniculate nucleus. **a:** Sagittal view. **b–f:** The slices indicate the position of the maps. **g:** Sagittal view of the ROI defining the corpus callosum. The coloring is used to color the fibers in Fig. 10a and b. For maps c–e in Fig. 10, only the part of the ROI between the two dashed lines was used.

In Vivo Data

The in vivo diffusion measurements were acquired on a Siemens 3T TIM Trio using an SE EPI sequence, with a TE of 95 ms and a TR of 8.5 s. *k*-Space was covered with 75% in the phase direction. The whole brain was covered with contiguous 2-mm slices in an in-plane resolution of $2 \times 2 \text{ mm}^2$. The diffusion encoding was performed in 61 directions with an effective *b*-value of 1000 s/mm^2 (30). Additionally, nine b_0 images were acquired without diffusion weighting. An online distortion correction method was applied according to Ref. 31. Additionally, a 3D T_1 magnetization prepared rapid gradient echo (MPRAGE) data set with a resolution of 1 mm^3 was acquired. The T_1 -weighted data set was segmented into WM, GM, and CSF using SPM5 (<http://www.fil.ion.ucl.ac.uk/spm>). A WM mask was created including all voxels with a value above 0.3 in the segmented WM probability maps. The WM mask was combined with the segmented GM mask to extract the transition between WM and GM, which was used as predefined border.

For the selection of specific fiber bundles, different ROIs were created as illustrated in Fig. 8. To identify the left primary motor cortex (M1), primary visual cortex (V1), and lateral geniculate nucleus (LGN), the T_1 -weighted data set was normalized to the MNI template using SPM5. The three different areas were extracted by the WFU PickAtlas Tool (32) and resliced to the coordinate system of the DW data set. The ROIs of M1 and V1 were enlarged about 4 mm and the small structure of the LGN to about 2 mm in each direction to access the WM. Additionally, several ROIs were created manually, as described in Ref. 33, to select the callosal fibers, cingulum (CG), arcuate fasciculus (AF), and inferior fronto-occipital fasciculus (IFO) (Fig. 8).

The Gibbs tracking method was applied to the whole brain, using a geometric cooling schedule with initial temperature $T_0 = 7 \times 10^4$, final temperature $T_f = 10^{-5}$, and iteration number $J = 5 \times 10^9$ iterations. The final configuration was used to extract the corticospinal tract (CST), callosal fibers, CG, AF, and IFO.

Extraction of the optical radiation (OR) was performed in a restricted volume (Fig. 9e–f) with the cylinder radius

$r_{\text{cyl}} = 0.2 \text{ mm}$ and the intensity of the Gibbs process $\beta = 0.7 \text{ mm}^{-4}$ to catch the thin structure of the OR. The initial and final temperatures were set to $T_0 = 10^4$ and $T_f = 10^{-5}$, respectively, with $J = 10^9$ iterations.

The whole-brain Gibbs tracking method was compared with the DTI-based FACT (34,35) method. The FACT method was applied to the in vivo data set by starting from the middle of each voxel inside the WM mask defined above. Fibers were selected using the ROI lying in the corpus callosum shown in Fig. 8c and g. The trajectories were colored depending on the anterior–posterior position, where the tracks pass the corpus callosum as shown in Fig. 8g. The results of the FACT and the Gibbs tracking methods are displayed in Fig. 10a and b, respectively.

A further comparison was performed among the FACT, PICO (16,17,36), and Gibbs tracking methods. For the PICO algorithm, a two-component MDT model was fitted to the data to estimate the orientation density function. This estimation was performed using look-up tables for the single-fiber case and for 40° , 50° , 60° , 70° , 80° , and 90° fiber crossings.

A comparison between resulted trajectories (FACT and Gibbs tracking) and probability maps (PICO) presents a problem. In our solution, the local connection probability is compared with the total length of reconstructed fibers inside a voxel. The maps obtained in this way were projected (by summation) on the coronal plane (Fig. 10c–e). This comparison takes into account all fibers that cross the corpus callosum in its central part, as illustrated in Fig. 8g. For all three methods, the same WM mask and the equivalent angle threshold were used as for the Gibbs tracking.

RESULTS

Curved Fibers

The Gibbs tracking method uses straight line segments to approximate all possible trajectories. The ability to reconstruct curved pathways is demonstrated using a simulated data set (Fig. 6c). The resulting course of the system energy during the optimization procedure is represented in Fig. 6b by the potential function f , calculated illustratively

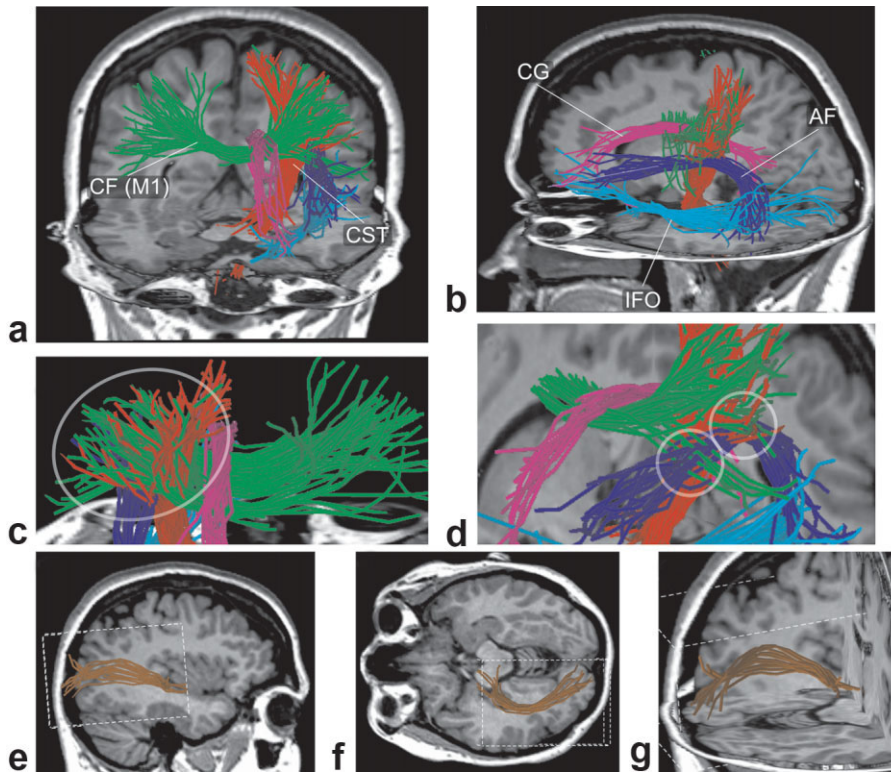


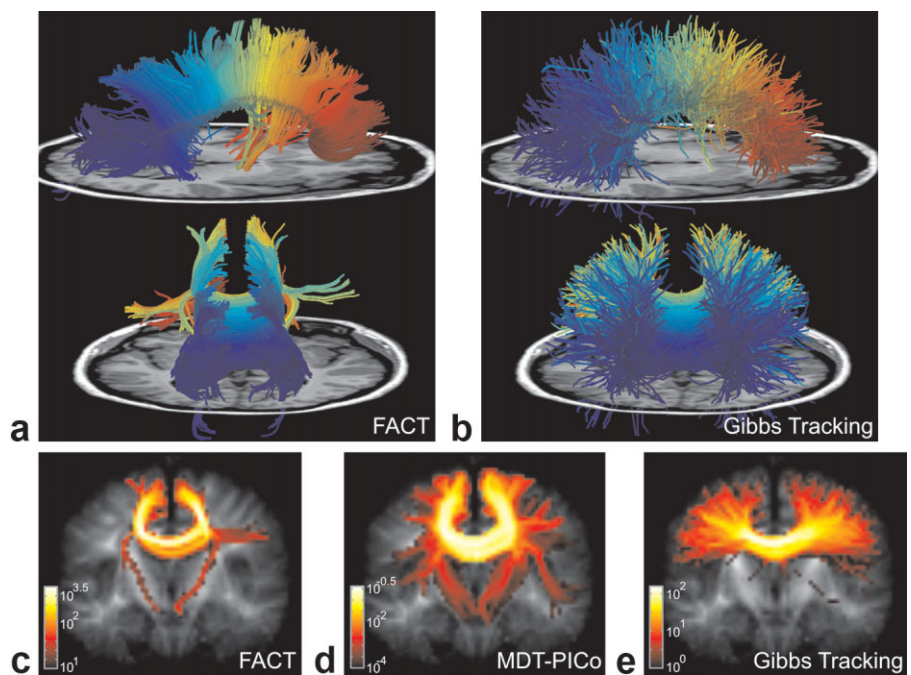
FIG. 9. Selected fiber pathways, reconstructed using Gibbs tracking. **a–d**: CF (green): Part of the callosal fibers coming from the left motor cortex. CST (red): Corticospinal tract. CG (magenta): Cingulum. AF (blue): Arcuate fasciculus. IFO (cyan): Inferior fronto-occipital fasciculus. **c**: Example of spreading fibers coming from the corpus callosum and the spinal cord. **d**: Example of fiber crossings between AF and CF, and between AF and CST. **e–g**: The extracted OR. The area indicated by the white box was reconstructed using Gibbs tracking with a smaller cylinder radius.

for temperature $T = 1$. The reconstructed trajectories were selected using four different ROIs and are displayed in Fig. 6c. The ROIs of both upper images were positioned at the outward region and, in contrast, the two ROIs of the images below were set to the inward region of the semi-circular fiber bundle. The selected trajectories stay mainly in their track and reach the corresponding voxel at the other end.

Crossing Fibers

The simulated phantom of crossing fibers is used to demonstrate the capability of Gibbs tracking to resolve crossings. Further, it is used to investigate how the cooling speed of the simulated annealing procedure affects the tracking results. The data energy U_D and the total energy $U_D + U_i$ for every final cylinder configuration depending

FIG. 10. Comparison of the callosal fibers reconstructed using different methods. In **a** and **b**, the callosal fibers reconstructed by the DTI-based FACT method (a) and the Gibbs tracking method (b) are shown as “spaghetti noodles.” The color coding of the fibers depends on where the fibers pass the corpus callosum, as defined in Fig. 8g. In **c–e**, the part of the callosal fibers passing the ROI defined in Fig. 8g between the two lines were reconstructed by FACT (c), PICo based on a two-component MDT model (d), and the Gibbs tracking method (e). They are visualized as probability maps. The values among the three maps are not comparable.



on the total number of iterations J are shown in Fig. 7a and b. The resulting trajectories using the schedule with $T_0 = 3 \times 10^3$, $T_f = 10^{-5}$, iterations are displayed in Fig. 7c. The ROIs were determined in a similar way as for the curved phantom; the trajectories were selected by the blue-marked ROIs and displayed on the four maps. Gibbs tracking was able to resolve the simulated crossing region and correctly reconstruct almost all fiber tracks as simulated.

Additionally, Gibbs tracking was applied to the phantom crossing fibers approximately 400 times with the geometric cooling schedule ($T_0 = 3 \times 10^3$, $T_f = 10^{-5}$, and $J = 2 \times 10^7$). The different weights w_f , w_s , and w_w were randomly varied in the interval from 1/2 to 2 times the standard value listed in Table 1 and used if they fulfilled the constraint $w_f \geq 2w_s$. A mean of 96.2% (standard deviation $\pm 4.0\%$) of the extracted fibers connected the two corresponding ROIs, 1.6% $\pm 2.3\%$ connected the wrong ROIs, and 2.2% $\pm 2.8\%$ of the fibers did not connect two of the ROIs and had at least one end not connected.

In Vivo Results

Processing the whole brain with $J = 5 \times 10^9$ iterations took approximately 1 month's calculation time on a standard PC. The following pathways were successfully extracted from the final configuration (Fig. 9a and b): the part of the callosal fibers connecting the primary motor cortex between the hemispheres (CF(M1)), the CST, the CG, the AF, and the IFO. The fanning and merging fibers of the CF(M1) and the CST are shown in Fig. 9c. The fiber crossings between the AF and the CST and between the AF and the CF(M1) are shown in Fig. 9d. The OR had an insufficient representation in this reconstruction, due to a cylinder density that was too low.

The OR was successfully reconstructed using a special calculation over a smaller area with the modified parameters described in the Materials and Methods section. The computations took approximately 5 days on a standard PC. All fibers were selected that pass through the LGN and V1, as illustrated in Fig. 9e–g.

The results of the comparison between the DTI-based FACT method and Gibbs tracking method are displayed in Fig. 10a and b. Caused by the projective pathway, nearly all fibers reconstructed by the DTI-FACT method are redirected in the vertical direction. In contrast, the Gibbs tracking method was able to resolve the crossing regions. The reconstructed fibers in Fig. 10b pass the crossing region and then spread out, contacting nearly the whole cortex. The coloring of the fibers is almost maintained near the cortex. This indicates that the position of the reconstructed fibers in the cortex reflects their anterior–posterior position in the corpus callosum.

In Fig. 10c–e the tracking of fibers passing the corpus callosum in the region delineated by the two lines in Fig 8g is compared for the DTI-based FACT method, the PICO method based on a two-component MDT model, and the Gibbs tracking method. The results are presented in the probability map style as described in the Materials and Methods section. Compared to the FACT method, the PICO method shows a significant improvement in covering the cortex by reaching more lateral areas. However, the U-shaped pathway connecting the part of the cortex that lies

in the medial region remains dominant. In contrast, the Gibbs tracking method covers the cortex nearly evenly.

DISCUSSION

In this work a new method for fiber tracking is presented that can reconstruct crossing and spreading fibers. An MDT model whose complexity is adapted automatically is used to describe the directional distribution of the apparent diffusion coefficient (ADC). The fitting of the MDT model and the fiber tracking are simultaneously performed by minimizing the global error. The good performance of the new approach was demonstrated using simulated data. As an in vivo verification, the major fiber pathways were successfully extracted. A dramatic difference for in vivo results was obtained as compared to the FACT and MDT-based PICO algorithms. Gibbs tracking was able to reconstruct spreading callosal fibers, covering an extensive fraction of WM and reaching a large area of the cortex.

In general, fiber tracking is very sensitive to local artifacts. Erroneous data in a few voxels might have global consequences for the restored neuronal pathways. In contrast, Gibbs tracking is based on the optimization of one global function. Thereby, it is able to overcome small local artifacts. For larger artifacts, the a priori constraints must be more strongly influenced by the different weights or the affected area has to be excluded from the likelihood function. However, weighting the a priori assumption more strongly might also lead to a higher insensitivity to local structures.

The choice of parameters for Gibbs tracking influences the resulting trajectories. The parameters can be divided into three groups. The first group of parameters describes the characteristics of fiber trajectories, such as the weights of the different energy terms (see also Table 1, type P). They are empirically adjusted in a self-consistent manner. In case the likelihood (data energy) and the a priori probability (interaction energy) do not contradict, the weights have a very low influence on the results. This was demonstrated using simulated crossing fibers. In the case of local artifacts, strong noise, or some diseases, there could be a mismatch between the different criteria. In this case, the weights used have a strong influence on the result. Further work is necessary to find an optimized set of weights for the different cases described above.

The second group of parameters describes the assumed properties of fiber bundles, such as the radius of the cylinders and the form of the anisotropic diffusion component contributed by a cylinder (Table 1, type A). In the present study, the latter was taken from the corpus callosum data. This assumption cannot be verified in other WM regions due to local differences in the fiber structure. For example, the defined radius of the cylinders strongly affects the number of tensor components of the adaptive MDT model inside a voxel, but it cannot be interpreted as real radius of the fiber bundle.

The third group contains parameters concerning the optimization process, such as the probability of occurrence of the different proposals or the shape and duration of the temperature schedule. They affect the speed of the convergence of the optimization process. They must be optimized to reduce computation time.

In the approach presented, an adaptive MDT model is used to describe the directional distribution of the ADC. The model is used in a direct way to calculate the DW signal given the fiber orientation. The typical number of tensor components is 16 for the in vivo results obtained in the whole brain. The number of tensor contributions directly depends on the chosen diameter of the cylinders. In contrast, other approaches (3,9,10) use the MDT model to solve the inverse problem (that is, to find the fiber orientation given the signal). For solving the inverse problem, the number of anisotropic tensor components should be restricted by two because of the numerical instability of fitting.

The main drawback of the current realization of the Gibbs tracking method is the long calculation time (~1 month on a standard PC for the in vivo results presented here). There are two possible ways to reduce the calculation time: reduce the mean computation time for one iteration, or reduce the number of iterations. The computation time for a single iteration can be strongly reduced by parallel computing. Conflicts between threads are expected to be rare because of the low fraction of cylinders in the total volume.

The number of iterations can be reduced by a more efficient temperature schedule, such as an adaptive schedule (18). A further possibility would be an optimization based on gradient descent with a random component. The Metropolis-Hastings algorithm currently used finds the optimal configuration and probes its environment. The latter goes beyond simple optimization and can be traded for performance when using the gradient descent. The results of the implementation of this method will be reported elsewhere.

The current method is compared with the DTI-based FACT and the MDT-based PICO algorithms. The FACT method is widely used in clinical fiber tracking by manufacturer's software and by stereotactic planning systems. The PICO method, based on MDT, was selected to compare with the present results, which also include the MDT model for resolving fiber crossings. The comparison demonstrates an essential difference (Fig. 10). The reconstructed fibers with the FACT method are redirected by the projective pathway. The PICO results show connection to the entire cortex with a strongly varying probability. Setting a higher threshold selects a few specific pathways. However, the result shows a trend to assign the highest probability to the U-shaped fibers similarly to the FACT algorithm. In contrast, Gibbs tracking results in a nearly uniform coverage of the WM and reaches large cortical regions.

This difference is surprising in view of the known equivalence between the random walk and the path integral approach in physics (37). The Monte Carlo random walk forms the basis of currently available methods for probabilistic tracking. The path integral operates directly with probabilities of individual random trajectories. The final local density of the random walker is determined by a single trajectory with the maximal probability, which is analogous to the fibers found with the Gibbs tracking. A proper comparison is complicated by the presence of numerous adjustable parameters in both methods and the rules of random walking, which are much more complex

than in simple physical systems. The issue of comparing Gibbs tracking with other methods will be addressed in future work.

In summary, Gibbs tracking can reconstruct crossing and spreading fiber configurations without interpolation or strong a priori constraints. The method is able to determine fiber pathways based on data acquired by using MR sequences, which are commonly used in clinical research. A significant reduction of computation time appears to be feasible, which is imperative for practical applications. This will enable a systematic in vivo exploration of the potential of the present method.

ACKNOWLEDGMENTS

We thank H. Burkhardt for productive suggestions; K.A. Il'yasov, S. Schnell, P. Gall, and J. Hennig for useful discussions; and J. Maclaren for his support concerning grammar and language.

REFERENCES

1. Moseley ME, Cohen Y, Kucharczyk J, Mintorovitch J, Asgari HS, Wendland MF, Tsuruda J, Norman D. Diffusion-weighted MR imaging of anisotropic water diffusion in cat central nervous system. *Radiology* 1990;176:439–445.
2. Stejskal EO, Tanner JE. Spin diffusion measurements—spin echoes in presence of a time-dependent field gradient. *J Chem Physics* 1965;42:288.
3. Tuch DS, Reese TG, Wiegell MR, Makris N, Belliveau JW, Wedeen VJ. High angular resolution diffusion imaging reveals intravoxel white matter fiber heterogeneity. *Magn Reson Med* 2002;48:577–582.
4. Behrens TE, Woolrich MW, Jenkinson M, Johansen-Berg H, Nunes RG, Clare S, Matthews PM, Brady JM, Smith SM. Characterization and propagation of uncertainty in diffusion-weighted MR imaging. *Magn Reson Med* 2003;50:1077–1088.
5. Jansons KM, Alexander DC. Persistent angular structure: new insights from diffusion magnetic resonance imaging data. *Inverse Problems* 2003;19:1031–1046.
6. Tuch DS, Reese TG, Wiegell MR, Wedeen VJ. Diffusion MRI of complex neural architecture. *Neuron* 2003;40:885–895.
7. Liu CL, Bammer R, Acar B, Moseley ME. Characterizing non-Gaussian diffusion by using generalized diffusion tensors. *Magn Reson Med* 2004;51:924–937.
8. Tournier JD, Calamante F, Gadian DG, Connelly A. Direct estimation of the fiber orientation density function from diffusion-weighted MRI data using spherical deconvolution. *Neuroimage* 2004;23:1176–1185.
9. Alexander DC. Multiple-fiber reconstruction algorithms for diffusion MRI. White matter in cognitive neuroscience: advances in diffusion tensor imaging and its applications. *Ann N Y Acad Sci* 2005;1064:113.
10. Kreher BW, Schneider JF, Mader I, Martin E, Hennig J, Il'yasov KA. Multitensor approach for analysis and tracking of complex fiber configurations. *Magn Reson Med* 2005;54:1216–1225.
11. Wedeen VJ, Hagmann P, Tseng WYI, Reese TG, Weisskoff RM. Mapping complex tissue architecture with diffusion spectrum magnetic resonance imaging. *Magn Reson Med* 2005;54:1377–1386.
12. Hosey T, Williams G, Ansoorge R. Inference of multiple fiber orientations in high angular resolution diffusion imaging. *Magn Reson Med* 2005;54:1480–1489.
13. Parker GJM, Alexander DC. Probabilistic anatomical connectivity derived from the microscopic persistent angular structure of cerebral tissue. *Phil Trans R Soc B Biol Sci* 2005;360:893–902.
14. Friman O, Farneback G, Westin CF. A Bayesian approach for stochastic white matter tractography. *IEEE Trans Med Imaging* 2006;25:965–978.
15. Kaden E, Knosche TR, Anwander A. Parametric spherical deconvolution: inferring anatomical connectivity using diffusion MR imaging. *Neuroimage* 2007;37:474–488.
16. Parker GJM, Haroon HA, Wheeler-Kingshott CAM. A framework for a streamline-based probabilistic index of connectivity (PICO) using a structural interpretation of MRI diffusion measurements. *J Magn Reson Imaging* 2003;18:242–254.

17. Parker GJ, Luzzi S, Alexander DC, Wheeler-Kingshott CA, Ciccarelli O, Lambon Ralph MA. Lateralization of ventral and dorsal auditory-language pathways in the human brain. *Neuroimage* 2005;24:656–666.
18. Perrin G, Descombes X, Zerubia J. Adaptive simulated annealing for energy minimization problem in a marked point process application. In: *Proc. Energy minimization methods in computer vision and pattern recognition. (EMMCVPR)*, St. Augustine, Fla, USA, 2005.
19. van Lieshout MNM. *Markov point processes and their applications*. London: Imperial College Press; 2000.
20. Stoica R, Descombes X, Zerubia J. A Gibbs point process for road extraction from remotely sensed images. *Int J Comput Vision* 2004;57:121–136.
21. Hastings WK. Monte-Carlo sampling methods using Markov chains and their applications. *Biometrika* 1970;57:97.
22. Geyer CJ, Moller J. Simulation procedures and likelihood inference for spatial point-processes. *Scand J Stat* 1994;21:359–373.
23. Geyer CJ. Likelihood inference for spatial point processes. In: Kendall WS, van Lieshout MNM, editors. *Stochastic geometry: likelihood and computation*. London: Chapman-Hall/CRC; 1998.
24. Metropolis N, Rosenbluth AW, Rosenbluth MN, Teller AH, Teller E. Equation of state calculations by fast computing machines. *J Chem Phys* 1953;21:1087–1092.
25. van Lieshout MNM. Stochastic annealing for nearest-neighbor point processes with application to object recognition. *Adv Appl Probabil* 1994;26:281–300.
26. Green PJ. Reversible jump Markov chain Monte Carlo computation and Bayesian model determination. *Biometrika* 1995;82:711–732.
27. Lacoste C, Descombes X, Zerubia J. Point processes for unsupervised line network extraction in remote sensing. *IEEE Trans Pattern Anal Mach Intell* 2005;27:1568–1579.
28. van Lieshout MNM, Stoica RS. The Candy model: properties and inference. *Stat Neerl* 2003;57:177–206.
29. Le Bihan D, Mangin JF, Poupon C, Clark CA, Pappata S, Molko N, Chabriet H. Diffusion tensor imaging: concepts and applications. *J Magn Reson Imaging* 2001;13:534–546.
30. Frank LR. Characterization of anisotropy in high angular resolution diffusion-weighted MRI. *Magn Reson Med* 2002;47:1083–1099.
31. Zaitsev M, Hennig J, Il'yasov K. Automated correction of EPI geometric distortions applied to diffusion tensor imaging. In: *Proceedings of the 14th Annual Meeting ISMRM*, Seattle, WA, USA, 2006 (Abstract 1024).
32. Maldjian JA, Laurienti PJ, Kraft RA, Burdette JH. An automated method for neuroanatomic and cytoarchitectonic atlas-based interrogation of fMRI data sets. *Neuroimage* 2003;19:1233–1239.
33. Mori S, Wakana S, Nagae-Poetscher LM, van Zijl PC. *MRI atlas of human white matter*. Amsterdam: Elsevier; 2005.
34. Mori S, Crain BJ, Chacko VP, van Zijl PC. Three-dimensional tracking of axonal projections in the brain by magnetic resonance imaging. *Ann Neurol* 1999;45:265–269.
35. Kreher BW, Hennig J, Il'yasov KA. DTI-FiberTools: a complete toolbox for DTI calculation, fiber tracking, and combined evaluation. In: *Proceedings of the 14th Annual Meeting ISMRM*, Seattle, WA, USA, 2006 (Abstract 2758).
36. Cook PA, Bai Y, Nedjati-Gilani S, Seunarine KK, Hall MG, Parker GJ, Alexander DC. Camino: Open-source diffusion-MRI reconstruction and processing. In: *Proceedings of the 14th Annual Meeting ISMRM*, Seattle, WA, USA, 2006 (Abstract 2759).
37. Feynman RP, Hibbs AR. *Quantum mechanics and path integrals*. New York: McGraw-Hill; 1965.